NANO LETTERS

pubs.acs.org/NanoLett Letter

Two-Dimensional Rare-Earth-Based Half-Metals with Topological Bimerons

Weiqi Liu, Xue He, Jianxiong Zhang, Fengshan Zheng, Yu-Jun Zhao, Rui Wu,* Jinbo Yang, Mathias Kläui, and Yanglong Hou*

Cite This: *Nano Lett.* 2024, 24, 15473−15480 Read Online

ACCESS | Metrics & More | Article Recommendations | Supporting Information

ABSTRACT: Two-dimensional magnets with spontaneous topological spin textures have important application prospects in highly integrated spintronic devices. However, so far, the predicted two-dimensional magnets with topological spin textures are mainly based on transition metals, and most of them are semiconductors or metals. Here, based on first-principles calculations, we predict two-dimensional rare-earth-based half-metallic monolayer GdA_2N_4 (A = Ge, Sn), with 100% spin polarization. Spontaneous topological spin textures, i.e., bimeron clusters, are revealed in those monolayers due to the magnetic frustration and easy-plane magnetic anisotropy. The bimeron clusters can be efficiently tuned through biaxial strain and driven by in-plane spin-polarized current. These results underscore the promising potential of rare-earth-based two-dimensional half-metals for spintronic device applications.

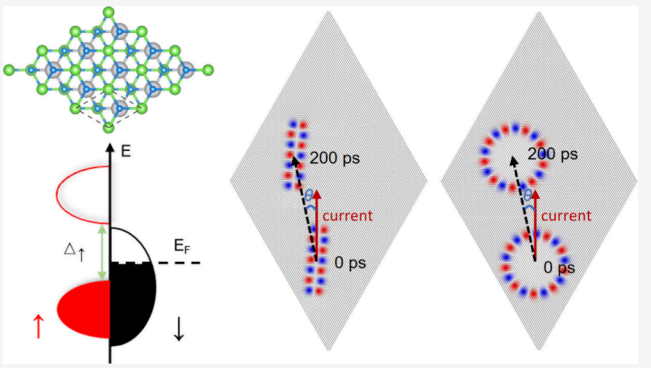

KEYWORDS: *rare-earth, two-dimensional magnets, half-metals, bimeron clusters*

Inspired by the pioneering work of monolayer van der Waals (vdW) materials CrI_3[1] and bilayer $Cr_2Ge_2Te_6$,[2] extensive research has been greatly stimulated on this type of materials. Results on a range of magnetic vdW magnets, such as VSe_2,[3] $CrPS_4$,[4] $CuCrP_2S_6$,[5] Fe_3GeTe_2,[6] and Fe_3GaTe_2,[7] have been reported, which provide an ideal research platform for low-dimensional magnetism. In the few-layer vdW magnets, large spin-filtering tunneling magnetoresistance,[8,9] strain-induced antiferromagnetic (AFM)−ferromagnetic (FM) transition and large electric field tunability of magnetism,[10,11] and the layer-number and twist-angle dependence of magnetism[1,12] have been reported, which is highly preferred in spintronic devices. Recently, various intriguing physical properties such as anomalous valley Hall effect,[13,14] topological spin textures,[15−17] and altermagnetism[18] in two-dimensional (2D) magnetic materials have also been reported and received widespread attention. For heterostructures of FM and AFM 2D materials, exchange bias has been explored.[19,20]

Various topologically nontrivial spin textures, such as skyrmions,[15,21] bimerons,[22,23] and hopfions,[24,25] are topologically stabilized and can be effectively manipulated,[26,27] making them promising information carriers for future high-density storage and information processing devices. Recently, great strides have been made to discover new topological spin textures in vdW or 2D magnets.[16,28−30] The magnetic skyrmions have been experimentally demonstrated in vdW ferromagnet Fe_3GeTe_2, Fe_5GeTe_2, and Fe_3GaTe_2 flakes.[16,17,30,31] Current-induced magnetic skyrmions or skyrmionium motion in Fe_3GaTe_2 flakes has also been observed at room temperature.[32,33] Besides, various monolayer systems have also been theoretically predicted to stabilize topological spin textures. For instance, spontaneous antiskyrmions are predicted in monolayer NiI_2 due to the magnetic frustration.[28] Meron-like topological spin textures have been predicted in XY-type magnet monolayer $CrCl_3$ as a result of the easy-plane magnetic anisotropy induced by magnetic dipole−dipole interaction.[34] However, so far, topological spin textures are mostly reported in magnetic semiconductors,[35−38] metals,[39−43] and insulators, while rarely reported in intrinsic half-metals, especially for 2D magnets. Topological spin textures can be more effectively driven by 100% spin-polarized current in half-metallic systems. So far, most 2D magnetic systems with topological spin textures are based on transition metals,[37,38,41] and the 4*f*-electron-based 2D magnetic systems that exhibit topological spin textures are still in demand. Theoretical studies suggest rare-earth-based 2D magnets show a large atomic magnetic moment and strong magnetic anisotro-

Received: October 23, 2024
Revised: November 17, 2024
Accepted: November 18, 2024
Published: November 21, 2024

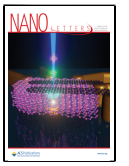

py,[44−49] which is crucial for spintronic device applications. Experimental studies have shown that the complex magnetic interactions of the 4*f* electron systems are the reason for the emergence of topological spin textures in rare-earth-based magnets.[50−52] For example, in a $Tb_6Co_{2.17}Si_{2.5}$ magnet,[52] the 4*f* electrons play an important role in the formation of (anti)meron chains. In $Tm_3Fe_5O_{12}$/Pt heterostructures,[53] skyrmions are stabilized by the interfacial Dzyaloshinskii−Moriya interaction (DMI). Therefore, exploring the topological spin textures in 2D magnetic systems based on rare-earth elements is of great significance.

Inspired by the successful synthesis of monolayer $MoSi_2N_4$,[54] which exhibits exotic physical properties,[55−58] here we explore and predict a new stable rare-earth-based monolayer, GdA_2N_4 (A = Ge, Sn). It is shown that monolayer GdA_2N_4 is an intrinsic XY-type FM half-metal with easy-plane magnetic anisotropy. Spontaneous bimerons are revealed using micromagnetic simulations, which is ascribed to the magnetic frustration and easy-plane magnetic anisotropy. Different types of bimerons are induced by biaxial strain. In addition, highly efficient electric-driven motion of bimeron clusters is achieved. Our results pave a new avenue for the future application of 2D rare-earth-based half-metallic materials in spintronics.

Monolayer GdA_2N_4 has a hexagonal crystal structure. According to the structure of the intermediate layer GdN_2, it can be categorized into 1T and 2H-GdA_2N_4 phases with *p*3*m*1 and *p*-6*m*2 space groups,[55] as illustrated in Figure 1(a) and

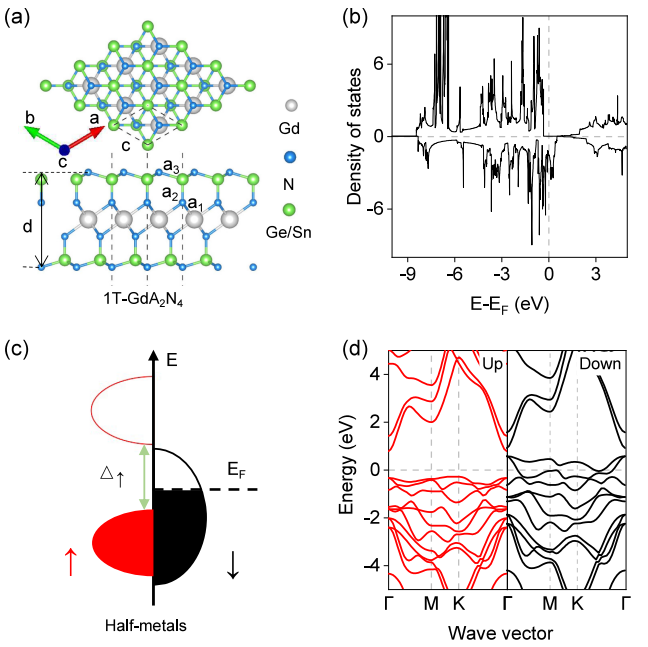

Figure 1. The electronic structure of the 1T-GdA_2N_4 monolayer: (a) the top and side views of the crystal structure, where the dashed box represents the primitive cell; (b) the DOS; (c) the schematic of DOS, where $\triangle_\uparrow$ represents bandgap values of the spin-up channel; (d) the spin resolved band structure.

Figure S2, respectively (see details of the calculation in the Supporting Information). First, we conduct complete structural optimization and calculate the relative energy and magnetic ground state of the 1T and 2H-GdA_2N_4 phases, respectively. The results are detailed in Table S2; both 1T and 2H-GdA_2N_4 phases exhibit an FM ground state, and the 1T phase has lower energy compared to the corresponding 2H phase. The energy difference between 1T and 2H phases is akin to that of dihalide monolayer MX_2 (M = Cr, Mn, Fe, Co and X = Cl, Br, I).[59] Therefore, unless otherwise specified, all study in the following is focused on the 1T phase. The lattice constants of monolayers $GdGe_2N_4$ and $GdSn_2N_4$ after optimization are 3.251 and 3.488 Å, respectively. The lattice constants increase proportionally with the element number of A (Ge → Sn). In addition, we calculate the cohesive energy, formation energy, elastic constants, phonon dispersion spectra, and ab initio molecular dynamics (AIMD) simulations of the system to confirm its stability, as shown in Figures S3−S5, providing guidance for experimental synthesis.

Based on the calculated stable structure of monolayer GdA_2N_4, we investigated the electronic and magnetic properties of the system. As shown in Figure S6, we construct three different magnetic configurations, i.e., FM, stripe-antiferromagnetic (s-AFM), and zigzag-antiferromagnetic (z-AFM) states. The results show that the energy difference $\Delta E = E_{z\text{-AFM}} - E_{FM}$ for monolayer $GdGe_2N_4$ and $GdSn_2N_4$ is 105.8 and 101.3 meV/f.u. (formula unit), respectively, exhibiting an FM ground state. As shown in Figure 1(b), the density of state (DOS) of monolayer $GdGe_2N_4$ is calculated, which shows that monolayer $GdGe_2N_4$ exhibits half-metallic properties. The Fermi level only crosses the spin-down channel, while the spin-up channel exhibits a bandgap, as shown in the schematic diagram in Figure 1(c). This characteristic is valuable for applications requiring 100% spin-polarized current, such as spin filters and spin valves. As shown in Figure 1(d), the spin-resolved band structure further confirms the half-metallic properties. The monolayer $GdSn_2N_4$ has similar half-metallic properties, except that the bandgap value of the spin-up channel is slightly smaller than that of monolayer $GdGe_2N_4$ (see Figure S7). In addition, the monolayer GdA_2N_4 has a total magnetic moment of 8 μ_B/f.u., which primarily originates from the spin magnetic moment of Gd-4*f* electrons, as shown in Figure S8 and Figure S9.

According to the Mermin−Wagner theorem,[60] magnetic anisotropy is crucial in the establishment of long-range magnetic ordering. Large magnetic anisotropy can counteract thermal fluctuations, thereby enhancing the durability of magnetic data storage. The magnitude of magnetic anisotropy can be represented by the magnetic anisotropy energy (MAE). Given the strong spin−orbit coupling (SOC) effect of the Gd atom, potentially resulting in a large MAE,[44] we calculate the MAE of monolayer GdA_2N_4 by using the formula $MAE = E_x - E_z$, where E_x and E_z represent the total energy of the magnetization direction along the in-plane *x* direction and out-of-plane *z* direction, respectively. The positive (negative) MAE indicates that the system shows easy-axis (easy-plane) magnetic anisotropy. As shown in Figure 2(a), MAE values along different angles θ within the *xy*, *yz*, and *xz* planes have been calculated. The relationship between MAE and rotation angle θ can be fitted using the equation $MAE(\theta) = K_1 \sin^2\theta + K_2 \sin^4\theta$, where K_1 and K_2 are magnetic anisotropy coefficients. As exhibited in Table S4, the negative K_1 indicates that the monolayer $GdGe_2N_4$ exhibits easy-plane magnetic anisotropy. In the *xy* plane, various magnetization orientations yield identical MAE, signifying the absence of an in-plane anisotropy within this system. Therefore, the monolayer $GdGe_2N_4$ can be classified as the 2D XY magnet.[46] As shown in Figure 2(b), the monolayer $GdGe_2N_4$ has −1290 μeV/f.u. magnetic anisotropy. The value is larger compared to

https://doi.org/10.1021/acs.nanolett.4c05268
Nano Lett. 2024, 24, 15473−15480

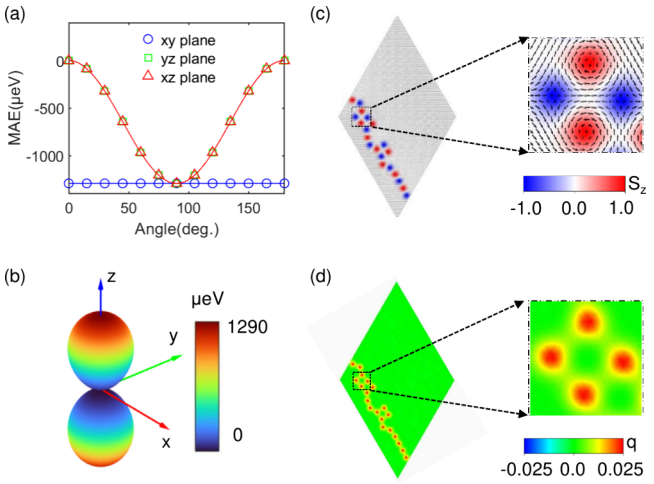

Figure 2. Magnetic anisotropy and the magnetic structures of monolayer $GdGe_2N_4$: (a) angular dependence of MAE in the *xy*, *yz*, and *xz* planes; (b) the MAE in the whole space; (c, d) topological spin textures and topological charge density at zero external magnetic field.

monolayer GdI_2 (−553 μeV/Gd)[44] and CeI_2 (−234 μeV/Ce).[46] The monolayer $GdSn_2N_4$ also belongs to the XY magnet and has a higher MAE (−2046 μeV/f.u.) than monolayer $GdGe_2N_4$, and the results are shown in Figure S10(a,b). Note that for thin film flakes, additionally a shape anisotropy contributes that also favors an easy-plane magnetic order.

The magnetic ordering temperature of the GdA_2N_4 system is studied next. Notably, monolayer GdA_2N_4 with an in-plane easy magnetization axis exhibits a Berezinskii−Kosterlitz−Thouless (BKT) magnetic phase transition.[61,62] The critical temperatures T_c of BKT magnetic transition can be estimated using the equation[63,64] $T_c = (0.89\Delta E)/(8k_B)$, where k_B is the Boltzmann constant. The estimated T_c values of monolayer $GdGe_2N_4$ and $GdSn_2N_4$ are 136.6 and 130.7 K, respectively, which are much larger than the T_c of the XY-type monolayer $CrCl_3$ (12 K)[34] and close to the T_c of the XY-type bilayer $NiPS_3$ (150 K).[65,66]

Typically, 2D materials with easy-plane magnetic anisotropy yield a residual SO(2) symmetry that usually leads to nonlinear spin textures, such as magnetic vortex and antivortex.[34] Through calculating the total energy of different magnetic configurations (detailed in Figure S6), the nearest neighbor and second nearest neighbor exchange coupling constants J_1 (J_2) of monolayer GdA_2N_4 are calculated; the results are detailed in Table S4. The frustration present in this system is due to the different signs of J_1 and J_2. The magnetic frustration ratio, defined as $|J_2|/J_1$, of monolayer $GdGe_2N_4$ and $GdSn_2N_4$ is about 0.33 and 0.32, respectively, which is slightly greater than the values of monolayer CrTeI (0.29) and MnPCl (0.27).[67] With considering both the strong easy-plane magnetic anisotropy and large magnetic frustration ratio, micromagnetic simulations reveal that monolayer GdA_2N_4 exhibits sponta-

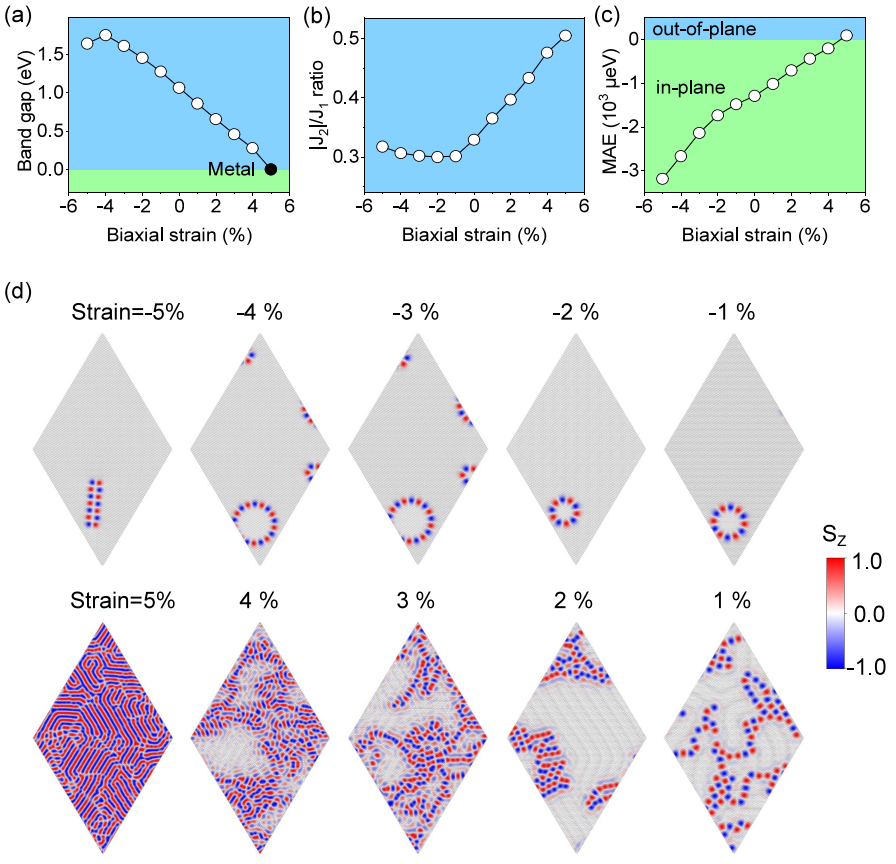

Figure 3. Biaxial strain dependence of the electronic and magnetic properties of the monolayer $GdGe_2N_4$: (a) strain dependence of the bandgap values of the spin-up channel (solid marker highlights the zero gap, i.e., the metallic state); (b) strain dependence of magnetic frustration ratio $|J_2|/J_1$; (c) strain dependence of the MAE; (d) strain dependence of topological spin textures at zero external magnetic field.

https://doi.org/10.1021/acs.nanolett.4c05268
Nano Lett. 2024, 24, 15473−15480

neous bimerons at zero magnetic field. As shown in Figure 2(c), the self-assembled antiparallel arranged bimerons are observed in monolayer $GdGe_2N_4$, which have also been reported in 2D magnetic systems, such as monolayer $CrCI_3$,[34] CrTeI, and MnPCl.[67] In addition, the bimerons in the monolayer $GdSn_2N_4$ exhibit a linear alignment (see Figure S10(c)). The topological charge density is defined as $q = \frac{1}{4\pi}\mathbf{S}\cdot(\partial_x\mathbf{S} \times \partial_y\mathbf{S})$.[68] The topological charge Q is defined as $Q = \int q\, dx\, dy$.[36] Figure 2(d) and Figure S10(d) show the distribution of topological charge density for monolayer GdA_2N_4; the bimerons with $Q = 1$ are composed of a pair of merons with $Q = 1/2$. As the topological counterpart of the skyrmions, bimerons carry an integer topological charge Q in the in-plane magnetized system.[27,69] In Figure S11, we conduct a more detailed discussion of the mechanism of magnetic frustration in this system and its effect on the formation of topological spin textures.

To tune the properties and, in particular, the spin textures, we investigate the impact of strain on the topological spin textures of the monolayer GdA_2N_4. First, we find that for biaxial strain as shown in Figure 3(a) and Figure S12(a), the bandgap value of the spin-up channel for monolayer GdA_2N_4 under compressive strain increases, indicating the enhancement of the half-metallic characteristics. However, the bandgap value of the spin-up channel for monolayer GdA_2N_4 decreases under tensile strain, leading to the transition of monolayer $GdGe_2N_4$ and $GdSn_2N_4$ from half-metals to normal metal states at a critical strain of 5% and 3%, respectively, as shown in Figure S13. In addition, as shown in Figure S14, the monolayer GdA_2N_4 maintains the FM ground state under different biaxial strain. Through calculating the total energy of different magnetic configurations, the corresponding magnetic frustration ratio values of monolayer GdA_2N_4 under varying biaxial strain are shown in Figure 3(b) and Figure S12(b). It is observed that the value increases to about 0.5 under a 5% tensile strain, while the value slightly decreases under compressive strain. Figure 3(c) shows the MAE of monolayer $GdGe_2N_4$ under varying biaxial strain. The MAE increases to about −3000 μeV/f.u. under −5% compressive strain, while the MAE decreases under tensile strain. It is worth noting that monolayer $GdGe_2N_4$ exhibits an MAE of 94 μeV/f.u. under 5% tensile strain, indicating a dominating perpendicular magnetic anisotropy (PMA) at this strain level. The MAE of monolayer $GdSn_2N_4$ under strain is similar to that of monolayer $GdGe_2N_4$, but its magnetic anisotropy remains in-plane, as shown in Figure S12(c). Through second-order perturbation theory analysis,[70] biaxial strain significantly affects the MAE of monolayer GdA_2N_4 by changing the matrix element difference (p_y, p_z) of the Gd atom. The specific results and discussion can be found in the Supporting Information and Figures S15−S17. As shown in Figure 3(d) and Figure S12(d), these unique topological spin textures can be significantly modified via biaxial strain.

The changes in the magnetic properties affect the stable spin textures. In particular, bimeron clusters can be induced under compressive strain through decreasing the magnetic frustration ratio and increasing the easy-plane magnetic anisotropy, while the tensile strain induces bimeron chains through increasing the magnetic frustration ratio and weakening the easy-plane magnetic anisotropy. Notably, due to the presence of PMA in monolayer $GdGe_2N_4$ under 5% tensile strain, a so-called Bloch line configuration is also stabilized, as shown in Figure 3(d). Figure S18 shows the topological charge density of monolayer GdA_2N_4 under a biaxial strain. Due to the presence of easy-plane magnetic anisotropy, it is worth noting that bimeron clusters with opposite signs of topological charge can coexist with each other.[71,72] The bimerons composed of a pair of merons $Q = -1/2$ are called antibimerons with $Q = -1$. The bimerons and antibimerons with the same absolute value of Q have different out-of-plane spin configurations.[73] Recent theories have predicted a topological spin texture hybrid-meron with a topological charge of $Q = 0$,[69] which still is topologically nontrivial due to the AFM coupling effect of interlayer bimerons. The influence of the dipole−dipole interaction on the topological spin textures under biaxial strain is also considered, as shown in Figure S19.

Two-dimensional half-metals can provide 100% spin-polarized current, which is crucial for efficient manipulation of topological spin textures. Thus, we further discuss the dynamics of topological spin textures caused by the spin-transfer torque.[74] The spin-transfer torque can simulate the in-plane spin-polarized current.[75] The motion of topological spin textures driven by in-plane current due to spin-transfer torques can be described by the Thiele equation:[26,76]

$$\mathbf{F} + \mathbf{G} \times (\mathbf{u} - \mathbf{v}) + \mathcal{D}(\beta\mathbf{u} - \alpha\mathbf{v}) = 0 \tag{1}$$

where $\mathbf{F}$ is the effective force.[77] $\mathbf{G} = (0, 0, -4\pi Q)$ is the gyromagnetic coupling vector.[73] $\mathbf{u}$ is the spin drift velocity related to spin-polarized current; $\mathbf{v}$ is the spin structure drift velocity; and β is the nonadiabaticity constant.[78] $\mathcal{D}$ is the dissipative force, where $\mathcal{D}_{ij} = \frac{1}{4\pi}\int dx\, dy\, \partial_i\mathbf{S}\cdot\partial_j\mathbf{S}$. When considering the direction of the spin-polarized current along the x axis, with $\mathbf{u}_y = \mathbf{0}$, the drift velocity component of the topological spin textures driven by the current is[24,75]

$$\mathbf{v}_x = \left(\frac{\beta}{\alpha} + \frac{G^2}{\alpha}\frac{\alpha - \beta}{G^2 + \alpha^2\mathcal{D}^2}\right)\mathbf{u}_x$$

$$\mathbf{v}_y = \left(\mathcal{D}G\frac{\alpha - \beta}{G^2 + \alpha^2\mathcal{D}^2}\right)\mathbf{u}_x \tag{2}$$

Note that topological spin textures will exhibit transverse motion induced by the Magnus force under the spin-polarized current, i.e., Hall-like effect.[27] The Hall angle is $\theta = \arctan(v_y/v_x)$. Here, we investigate the dynamics of bimeron clusters under spin-polarized current. The consistency between the analytical results and numerical results is verified through the simulation results of isolated bimerons, as shown in Figure S20. Figure 4(a−h) show snapshots of the topological spin textures of monolayer GdA_2N_4 with bimeron clusters under different biaxial strain driven by spin-polarized current along the y axis. The topological spin textures with different topological charge numbers all exhibit a linear motion trajectory. However, it is worth noting that the opposite Q signs lead to opposite transverse velocity v_x. As shown in Figure 4(a) and Figure S21, the bimeron clusters with negative topological charge numbers are subjected to a Magnus force to the right, resulting in a drift velocity component v_x to the right. In contrast, for bimeron clusters with positive topological charge numbers (see Figure 4(b−h)), they are subjected to a Magnus force to the left during the drift process, resulting in a drift velocity component v_x to the left. As shown in Figure 4(i), it can be seen that although the absolute values of the drift velocity components of bimeron clusters with different topological charge numbers are slightly different, the absolute

https://doi.org/10.1021/acs.nanolett.4c05268
Nano Lett. 2024, 24, 15473−15480

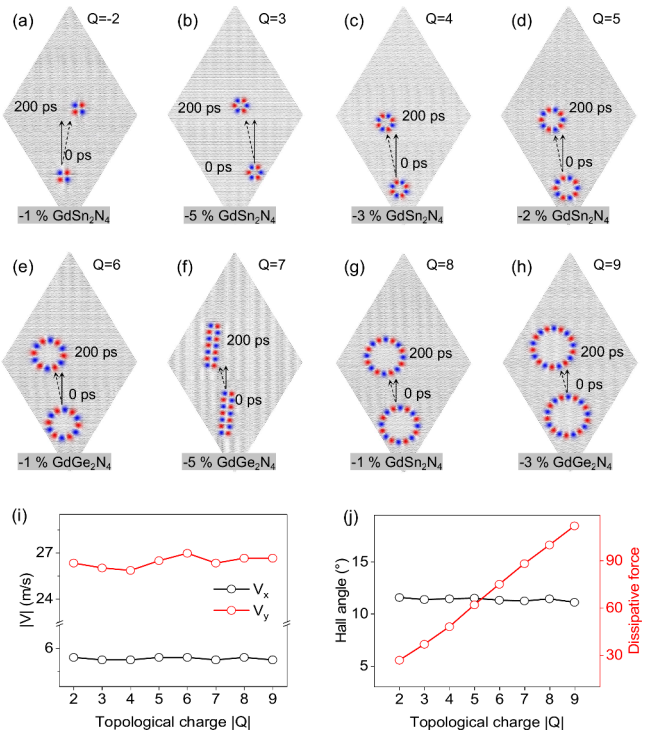

Figure 4. The spin-polarized current driven motion of the bimeron clusters in half-metallic monolayer GdA_2N_4 under different biaxial strain at zero external field: (a–h) the snapshots of the bimeron clusters driven by 100% spin-polarized current along the *y* axis, where the solid line represents the direction of spin-polarized current, and the dotted line represents the direction of topological spin texture drift; (i) the drift velocity component along *x* and *y* directions; (j) the Hall angle and dissipative force of the bimeron clusters with different topological charges *Q*.

values of Hall angle for all bimeron clusters are within the range of 11° to 11.6° (see Figure 4(j)), indicating that the bimeron Hall effect does not depend strongly on the size and shape. According to formula 2, the Hall angle of the system is determined by $\frac{\mathcal{D}}{G}$. As shown in Figure 4(j), the dissipation force $\mathcal{D}$ is proportional to the topological charge *Q*; therefore, the bimeron clusters with different topological charge numbers exhibit a similar Hall angle. In addition, the influence of the nonadiabaticity constant β on the Hall angle is also discussed, as shown in Figures S22 and S23.

Based on the above results analysis, with applying spin-polarized current in an appropriate direction, the collision between bimeron clusters with opposite signs of the topological charge can be achieved. The Figure S24(a–f) show snapshots of the topological spin textures of monolayer $GdGe_2N_4$ under −3% compressive strain driven by spin-polarized current, the bimeron clusters with topological charge $Q = 9$ and −3 collide and the system energy undergoes a drastic change between 200 and 300 ns (see Figure S24(g)), indicating the collision and merging between the bimeron clusters with opposite topological charge signs and resulting in the new bimeron clusters with topological charge $Q = 6$. It is worth noting that this process entails topological charge number conservation in the system, as shown in Figure S24(h).

With these findings, we show the stability of bimerons in monolayer GdA_2N_4 systems with half-metallic properties. The dynamics due to injected fully polarized currents as analyzed within the Thiele model shows that bimeron clusters with different topological charge numbers exhibit a similar Hall effect, and collision and merging between the spin textures can be achieved through injection of currents while conserving the overall topological winding number of the system.

To summarize, we use first-principles calculations to predict monolayer GdA_2N_4 with a seven atom layer structure and systematically study its stability and electronic and magnetic properties. It is found that monolayer GdA_2N_4 exhibits half-metallicity and easy-plane magnetic anisotropy. Monolayer GdA_2N_4 exhibits spontaneous bimerons, which are induced by magnetic frustration and easy-plane magnetic anisotropy. The morphology of the topological spin textures can be efficiently tuned through applied biaxial strain. The half-metallic electronic structure naturally lends the system to manipulation by injected currents. The dynamics of micromagnetic simulations indicate that the bimeron clusters show a linear motion under injected spin-polarized currents. The absolute value of the bimeron Hall angle does not depend strongly on the size and shape. In addition, new bimeron clusters can be obtained through collision and merging between bimeron clusters that could be useful for complex computational approaches. With the above intriguing properties, the predicted rare-earth 2D magnets with half-metallic properties are particularly promising for spintronic devices like spin-transfer torque driven magnetic tunneling junction and racetrack memories.

■ ASSOCIATED CONTENT

Supporting Information

The Supporting Information is available free of charge at https://pubs.acs.org/doi/10.1021/acs.nanolett.4c05268.

Details of the computational methods; the optimized crystal structure parameters and relative energies of 1T and 2H-GdA_2N_4 phases; the stability and mechanical properties of monolayer GdA_2N_4; magnetic configurations and magnetic parameter; electronic properties of monolayer GdA_2N_4; angular dependence of MAE and topological spin textures of monolayer $GdSn_2N_4$; the mechanism of magnetic frustration; spin-resolved band structure, magnetic frustration ratio, total energy, MAE, and topological spin textures of monolayer GdA_2N_4 under biaxial strain; the bimeron clusters of monolayer GdA_2N_4 under −3% compressive strain and isolated bimerons driven by spin-polarized current; the influence of damping parameter α and nonadiabaticity constant β on Hall angle; the collision and merging of two bimeron clusters driven by spin-polarized current (PDF)

■ AUTHOR INFORMATION

Corresponding Authors

Rui Wu − *Spin-X Institute, School of Physics and Optoelectronics, and State Key Laboratory of Luminescent Materials and Devices, South China University of Technology, Guangzhou 511442, China;* orcid.org/0000-0003-2010-5961; Email: ruiwu001@scut.edu.cn

Yanglong Hou − *School of Materials, Shenzhen Campus of Sun Yat-Sen University, Shenzhen 518107, China; School of Materials Science and Engineering, Beijing Key Laboratory for Magnetoelectric Materials and Devices, Peking University, Beijing 100871, China;* orcid.org/0000-0003-0579-4594; Email: hou@sysu.edu.cn

https://doi.org/10.1021/acs.nanolett.4c05268
Nano Lett. 2024, 24, 15473−15480

Authors

Weiqi Liu − *Spin-X Institute and School of Physics and Optoelectronics, South China University of Technology, Guangzhou 511442, China*

Xue He − *Spin-X Institute and School of Physics and Optoelectronics, South China University of Technology, Guangzhou 511442, China*

Jianxiong Zhang − *Spin-X Institute and School of Physics and Optoelectronics, South China University of Technology, Guangzhou 511442, China*

Fengshan Zheng − *Spin-X Institute, School of Physics and Optoelectronics, and State Key Laboratory of Luminescent Materials and Devices, South China University of Technology, Guangzhou 511442, China;* orcid.org/0000-0001-7354-041X

Yu-Jun Zhao − *School of Physics and Optoelectronics, South China University of Technology, Guangzhou 511442, China;* orcid.org/0000-0002-6923-1099

Jinbo Yang − *State Key Laboratory for Mesoscopic Physics, School of Physics, Peking University, Beijing 100871, China;* orcid.org/0000-0003-3517-9701

Mathias Kläui − *Institute of Physics, Johannes Gutenberg-University Mainz, Mainz 55128, Germany*

Complete contact information is available at: https://pubs.acs.org/10.1021/acs.nanolett.4c05268

Notes

The authors declare no competing financial interest.

■ ACKNOWLEDGMENTS

This work is supported by the National Key R&D Program of China (Grant Nos. 2022YFA1203902, 2022YFA1200093), the National Natural Science Foundation of China (NSFC) (Grant Nos. 12241401, 12374108, 12104052, 52373226, 52027801, 92263203), the China-Germany Collaboration Project (M-0199), the Guangdong Provincial Quantum Science Strategic Initiative (Grant No. GDZX2401002), the Fundamental Research Funds for the Central Universities, the State Key Lab of Luminescent Materials and Devices, South China University of Technology, and the GBRCE for Functional Molecular Engineering. We acknowledge support by the German Research Foundation (CRC TRR 288-422213477 Project A12). This work is partially supported by the High Performance Computing Platform of South China University of Technology.

■ REFERENCES

(1) Huang, B.; Clark, G.; Navarro-Moratalla, E.; et al. Layer-dependent ferromagnetism in a van der Waals crystal down to the monolayer limit. *Nature* **2017**, *546* (7657), 270−273.

(2) Gong, C.; Li, L.; Li, Z.; et al. Discovery of intrinsic ferromagnetism in two-dimensional van der Waals crystals. *Nature* **2017**, *546* (7657), 265−269.

(3) Bonilla, M.; Kolekar, S.; Ma, Y.; et al. Strong room-temperature ferromagnetism in VSe_2 monolayers on van der Waals substrates. *Nat. Nanotechnol.* **2018**, *13* (4), 289−293.

(4) Wu, R.; Ross, A.; Ding, S.; et al. Magnetotransport study of van der Waals $CrPS_4$/(Pt, Pd) heterostructures: Spin-flop transition and room-temperature anomalous Hall effect. *Phys. Rev. Appl.* **2022**, *17* (6), 064038.

(5) Wang, X.; Shang, Z.; Zhang, C.; et al. Electrical and magnetic anisotropies in van der Waals multiferroic $CuCrP_2S_6$. *Nat. Commun.* **2023**, *14* (1), 840.

(6) Fei, Z.; Huang, B.; Malinowski, P.; et al. Two-dimensional itinerant ferromagnetism in atomically thin Fe_3GeTe_2. *Nat. Mater.* **2018**, *17* (9), 778−782.

(7) Zhang, G.; Guo, F.; Wu, H.; et al. Above-room-temperature strong intrinsic ferromagnetism in 2D van der Waals Fe_3GaTe_2 with large perpendicular magnetic anisotropy. *Nat. Commun.* **2022**, *13* (1), 5067.

(8) Song, T.; Cai, X.; Tu, M. W.; et al. Giant tunneling magnetoresistance in spin-filter van der Waals heterostructures. *Science* **2018**, *360* (6394), 1214−1218.

(9) Song, T.; Tu, M. W.; Carnahan, C.; et al. Voltage control of a van der Waals spin-filter magnetic tunnel junction. *Nano Lett.* **2019**, *19* (2), 915−920.

(10) Jiang, S.; Li, L.; Wang, Z.; et al. Controlling magnetism in 2D CrI_3 by electrostatic doping. *Nat. Nanotechnol.* **2018**, *13* (7), 549−553.

(11) Jiang, S.; Shan, J.; Mak, K. F. Electric-field switching of two-dimensional van der Waals magnets. *Nat. Mater.* **2018**, *17* (5), 406−410.

(12) Xu, Y.; Ray, A.; Shao, Y.-T.; et al. Coexisting ferromagnetic−antiferromagnetic state in twisted bilayer CrI_3. *Nat. Nanotechnol.* **2022**, *17* (2), 143−147.

(13) Tong, W.-Y.; Gong, S.-J.; Wan, X.; et al. Concepts of ferrovalley material and anomalous valley Hall effect. *Nat. Commun.* **2016**, *7* (1), 13612.

(14) Zhao, P.; Ma, Y.; Lei, C., et al. Single-layer $LaBr_2$: Two-dimensional valleytronic semiconductor with spontaneous spin and valley polarizations. *Appl. Phys. Lett.*, **2019**, *115* (26), 261605.

(15) Ding, B.; Li, Z.; Xu, G.; et al. Observation of magnetic skyrmion bubbles in a van der Waals ferromagnet Fe_3GeTe_2. *Nano Lett.* **2020**, *20* (2), 868−873.

(16) Birch, M. T.; Powalla, L.; Wintz, S.; et al. History-dependent domain and skyrmion formation in 2D van der Waals magnet Fe_3GeTe_2. *Nat. Commun.* **2022**, *13* (1), 3035.

(17) Liu, C.; Zhang, S.; Hao, H.; et al. Magnetic skyrmions above room temperature in a van der Waals ferromagnet Fe_3GaTe_2. *Adv. Mater.* **2024**, *36* (18), 2311022.

(18) Zhu, Y.; Chen, T.; Li, Y.; et al. Multipiezo effect in altermagnetic V_2SeTeO monolayer. *Nano Lett.* **2024**, *24* (1), 472−478.

(19) Puthirath Balan, A.; Kumar, A.; Reiser, P.; et al. Identifying the origin of thermal modulation of exchange bias in $MnPS_3/Fe_3GeTe_2$ van der Waals heterostructures. *Adv. Mater.* **2024**, *36*, 2403685.

(20) Puthirath Balan, A.; Kumar, A.; Scholz, T.; et al. Harnessing van der Waals $CrPS_4$ and surface oxides for nonmonotonic preset field induced exchange bias in Fe_3GeTe_2. *ACS Nano* **2024**, *18* (11), 8383−8391.

(21) Chakraborty, A.; Srivastava, A. K.; Sharma, A. K.; et al. Magnetic skyrmions in a thickness tunable 2D ferromagnet from a defect driven Dzyaloshinskii−Moriya interaction. *Adv. Mater.* **2022**, *34* (11), 2108637.

(22) Sun, W.; Wang, W.; Li, H.; et al. $LaBr_2$ bilayer multiferroic moiré superlattice with robust magnetoelectric coupling and magnetic bimerons. *npj Comput. Mater.* **2022**, *8* (1), 159.

(23) Bhukta, M.; Dohi, T.; Bharadwaj, V. K.; et al. Homochiral antiferromagnetic merons, antimerons and bimerons realized in synthetic antiferromagnets. *Nat. Commun.* **2024**, *15* (1), 1641.

(24) Wang, X. S.; Qaiumzadeh, A.; Brataas, A. Current-driven dynamics of magnetic hopfions. *Phys. Rev. Lett.* **2019**, *123* (14), 147203.

(25) Zheng, F.; Kiselev, N. S.; Rybakov, F. N.; et al. Hopfion rings in a cubic chiral magnet. *Nature* **2023**, *623* (7988), 718−723.

(26) Jiang, W.; Zhang, X.; Yu, G.; et al. Direct observation of the skyrmion Hall effect. *Nat. Phys.* **2017**, *13* (2), 162−169.

(27) Shen, L.; Li, X.; Xia, J.; et al. Dynamics of ferromagnetic bimerons driven by spin currents and magnetic fields. *Phys. Rev. B* **2020**, *102* (10), 104427.

(28) Amoroso, D.; Barone, P.; Picozzi, S. Spontaneous skyrmionic lattice from anisotropic symmetric exchange in a Ni-halide monolayer. *Nat. Commun.* **2020**, *11* (1), 5784.
(29) Grebenchuk, S.; Mckeever, C.; Grzeszczyk, M.; et al. Topological spin textures in an insulating van der Waals ferromagnet. *Adv. Mater.* **2024**, *36* (24), 2311949.
(30) Lv, X.; Lv, H.; Huang, Y.; et al. Distinct skyrmion phases at room temperature in two-dimensional ferromagnet Fe_3GaTe_2. *Nat. Commun.* **2024**, *15* (1), 3278.
(31) Schmitt, M.; Denneulin, T.; Kovács, A.; et al. Skyrmionic spin structures in layered Fe_5GeTe_2 up to room temperature. *Commun. Phys.* **2022**, *5* (1), 254.
(32) Ji, Y.; Yang, S.; Ahn, H.-B.; et al. Direct observation of room-temperature magnetic skyrmion motion driven by ultra-low current density in van der Waals ferromagnets. *Adv. Mater.* **2024**, *36* (21), 2312013.
(33) Zhang, H.; Shao, Y.-T.; Chen, X.; et al. Spin disorder control of topological spin texture. *Nat. Commun.* **2024**, *15* (1), 3828.
(34) Lu, X.; Fei, R.; Zhu, L.; et al. Meron-like topological spin defects in monolayer $CrCl_3$. *Nat. Commun.* **2020**, *11* (1), 4724.
(35) Shen, Z.; Xue, Y.; Wu, Z.; et al. Enhanced Curie temperature and skyrmion stability by strain in room temperature ferromagnetic semiconductor CrISe monolayer. *Appl. Phys. Lett.* **2022**, *121* (20), 202402.
(36) Du, W.; Dou, K.; He, Z.; et al. Spontaneous magnetic skyrmions in single-layer $CrInX_3$ (X = Te, Se). *Nano Lett.* **2022**, *22* (8), 3440−3446.
(37) Gorkan, T.; Das, J.; Kapeghian, J.; et al. Skyrmion formation in Ni-based Janus dihalide monolayers: Interplay between magnetic frustration and Dzyaloshinskii-Moriya interaction. *Phys. Rev. Mater.* **2023**, *7* (5), 054006.
(38) Wang, Z.-Q.; Xue, F.; Qiu, L.; et al. Switching intrinsic magnetic skyrmions with controllable magnetic anisotropy in van der Waals multiferroic heterostructures. *Nano Lett.* **2024**, *24* (14), 4117−4123.
(39) Mühlbauer, S.; Binz, B.; Jonietz, F.; et al. Skyrmion lattice in a chiral magnet. *Science* **2009**, *323* (5916), 915−919.
(40) Soumyanarayanan, A.; Raju, M.; Gonzalez Oyarce, A. L.; et al. Tunable room-temperature magnetic skyrmions in Ir/Fe/Co/Pt multilayers. *Nat. Mater.* **2017**, *16* (9), 898−904.
(41) Xu, C.; Chen, P.; Tan, H.; et al. Electric-field switching of magnetic topological charge in type-I multiferroics. *Phys. Rev. Lett.* **2020**, *125* (3), 037203.
(42) Yuan, J.; Yang, Y.; Cai, Y.; et al. Intrinsic skyrmions in monolayer Janus magnets. *Phys. Rev. B* **2020**, *101* (9), 094420.
(43) Liang, J.; Wang, W.; Du, H.; et al. Very large Dzyaloshinskii-Moriya interaction in two-dimensional Janus manganese dichalcogenides and its application to realize skyrmion states. *Phys. Rev. B* **2020**, *101* (18), 184401.
(44) Wang, B.; Zhang, X.; Zhang, Y.; et al. Prediction of a two-dimensional high-T_C f-electron ferromagnetic semiconductor. *Mater. Horiz.* **2020**, *7* (6), 1623−1630.
(45) Tan, H.; Shan, G.; Zhang, J. Prediction of novel two-dimensional room-temperature ferromagnetic rare-earth material - GdB_2N_2 with large perpendicular magnetic anisotropy. *Mater. Today Phys.* **2022**, *24*, 100700.
(46) Sheng, K.; Chen, Q.; Yuan, H.-K.; et al. Monolayer CeI_2: An intrinsic room-temperature ferrovalley semiconductor. *Phys. Rev. B* **2022**, *105* (7), 075304.
(47) You, H.; Ding, N.; Chen, J.; et al. Gadolinium halide monolayers: a fertile family of two-dimensional 4f magnets. *ACS Appl. Electron. Mater.* **2022**, *4* (7), 3168−3176.
(48) Sheng, K.; Yuan, H. K.; Wang, Z. Y. Monolayer gadolinium halides, GdX_2 (X = F, Cl, Br): intrinsic ferrovalley materials with spontaneous spin and valley polarizations. *Phys. Chem. Chem. Phys.* **2022**, *24* (6), 3865−3874.
(49) Bai, Y.; Wu, Y.; Jia, C.; et al. Two-dimensional 4f magnetic $EuSn_2X_2$ (X = P, As) monolayers: A first-principles study. *Appl. Phys. Lett.* **2023**, *123* (1), 012401.
(50) Hirschberger, M.; Nakajima, T.; Gao, S.; et al. Skyrmion phase and competing magnetic orders on a breathing kagomé lattice. *Nat. Commun.* **2019**, *10* (1), 5831.
(51) Ye, C.; Li, L.-L.; Shu, Y.; et al. Generation and manipulation of skyrmions and other topological spin structures with rare metals. *Rare Met.* **2022**, *41* (7), 2200−2216.
(52) Xu, J.; Wang, L.; Xi, L.; et al. Spontaneous topological (anti)Meron chains in the domain walls of centrosymmetric rare-earth magnet. *Adv. Funct. Mater.* **2024**, *34* (22), 2314127.
(53) Shao, Q.; Liu, Y.; Yu, G.; et al. Topological Hall effect at above room temperature in heterostructures composed of a magnetic insulator and a heavy metal. *Nat. Electron.* **2019**, *2* (5), 182−186.
(54) Hong, Y. L.; Liu, Z.; Wang, L.; et al. Chemical vapor deposition of layered two-dimensional $MoSi_2N_4$ materials. *Science* **2020**, *369* (6504), 670−674.
(55) Mortazavi, B.; Javvaji, B.; Shojaei, F.; et al. Exceptional piezoelectricity, high thermal conductivity and stiffness and promising photocatalysis in two-dimensional $MoSi_2N_4$ family confirmed by first-principles. *Nano Energy* **2021**, *82*, 105716.
(56) Wang, L.; Shi, Y.; Liu, M.; et al. Intercalated architecture of MA_2Z_4 family layered van der Waals materials with emerging topological, magnetic and superconducting properties. *Nat. Commun.* **2021**, *12* (1), 2361.
(57) He, C.; Xu, C.; Chen, C.; et al. Unusually high thermal conductivity in suspended monolayer $MoSi_2N_4$. *Nat. Commun.* **2024**, *15* (1), 4832.
(58) Latychevskaia, T.; Bandurin, D. A.; Novoselov, K. S. A new family of septuple-layer 2D materials of $MoSi_2N_4$-like crystals. *Nat. Rev. Phys.* **2024**, *6* (7), 426−438.
(59) Kulish, V. V.; Huang, W. Single-layer metal halides MX_2 (X = Cl, Br, I): stability and tunable magnetism from first principles and Monte Carlo simulations. *J. Mater. Chem. C* **2017**, *5* (34), 8734−8741.
(60) Mermin, N. D.; Wagner, H. Absence of ferromagnetism or antiferromagnetism in one- or two-dimensional isotropic Heisenberg models. *Phys. Rev. Lett.* **1966**, *17* (22), 1133−1136.
(61) Zhang, S.; Xu, R.; Duan, W.; et al. Intrinsic half-metallicity in 2D ternary chalcogenides with high critical temperature and controllable magnetization direction. *Adv. Funct. Mater.* **2019**, *29* (14), 1808380.
(62) Ashton, M.; Gluhovic, D.; Sinnott, S. B.; et al. Two-dimensional intrinsic half-metals with large spin gaps. *Nano Lett.* **2017**, *17* (9), 5251−5257.
(63) Ma, A. N.; Wang, P. J.; Zhang, C. W. Intrinsic ferromagnetism with high temperature, strong anisotropy and controllable magnetization in the CrX (X = P, As) monolayer. *Nanoscale* **2020**, *12* (9), 5464−5470.
(64) Frey, N. C.; Kumar, H.; Anasori, B.; et al. Tuning noncollinear spin structure and anisotropy in ferromagnetic nitride MXenes. *ACS Nano* **2018**, *12* (6), 6319−6325.
(65) Kim, K.; Lim, S. Y.; Lee, J.-U.; et al. Suppression of magnetic ordering in XXZ-type antiferromagnetic monolayer $NiPS_3$. *Nat. Commun.* **2019**, *10* (1), 345.
(66) Kang, S.; Kim, K.; Kim, B. H.; et al. Coherent many-body exciton in van der Waals antiferromagnet $NiPS_3$. *Nature* **2020**, *583* (7818), 785−789.
(67) Li, P.; Yu, D.; Liang, J.; et al. Topological spin textures in 1T-phase Janus magnets: Interplay between Dzyaloshinskii-Moriya interaction, magnetic frustration, and isotropic higher-order interactions. *Phys. Rev. B* **2023**, *107* (5), 054408.
(68) Berg, B.; Lüscher, M. Definition and statistical distributions of a topological number in the lattice O(3) σ-model. *Nucl. Phys. B* **1981**, *190* (2), 412−424.
(69) Du, W. H.; He, Z. L.; Dou, K. Y.; et al. Chiral magnetic quasiparticles with zero topological charge in 2D lattice. *Adv. Funct. Mater.* **2024**, *34*, 2400971.
(70) Wang, D.-S.; Wu, R.; Freeman, A. J. First-principles theory of surface magnetocrystalline anisotropy and the diatomic-pair model. *Phys. Rev. B* **1993**, *47* (22), 14932−14947.

https://doi.org/10.1021/acs.nanolett.4c05268
Nano Lett. 2024, 24, 15473−15480

(71) Moon, K.-W.; Yoon, J.; Kim, C.; et al. Existence of in-plane magnetic skyrmion and its motion under current flow. *Phys. Rev. Appl.* **2019**, *12* (6), 064054.
(72) Sun, W.; Wang, W.; Li, H.; et al. Controlling bimerons as skyrmion analogues by ferroelectric polarization in 2D van der Waals multiferroic heterostructures. *Nat. Commun.* **2020**, *11* (1), 5930.
(73) Zhang, X.; Xia, J.; Shen, L.; et al. Static and dynamic properties of bimerons in a frustrated ferromagnetic monolayer. *Phys. Rev. B* **2020**, *101* (14), 144435.
(74) Zhang, S.; Li, Z. Roles of nonequilibrium conduction electrons on the magnetization dynamics of ferromagnets. *Phys. Rev. Lett.* **2004**, *93* (12), 127204.
(75) Menezes, R. M.; Mulkers, J.; Silva, C. C. D. S.; et al. Deflection of ferromagnetic and antiferromagnetic skyrmions at heterochiral interfaces. *Phys. Rev. B* **2019**, *99* (10), 104409.
(76) Thiele, A. A. Steady-state motion of magnetic domains. *Phys. Rev. Lett.* **1973**, *30* (6), 230−233.
(77) Han, S. U.; Kim, W.; Kim, S. K.; et al. Tunable domain-wall skyrmion Hall effect driven by a current and a magnetic field. *Phys. Rev. B* **2024**, *109* (1), 014404.
(78) Boulle, O.; Malinowski, G.; Kläui, M. Current-induced domain wall motion in nanoscale ferromagnetic elements. *Mater. Sci. Eng. R Rep.* **2011**, *72* (9), 159−187.

https://doi.org/10.1021/acs.nanolett.4c05268
Nano Lett. 2024, 24, 15473−15480